RESEARCH OUTPUTS / RÉSULTATS DE RECHERCHE

Higher Catalytic Activity of Pd Monolayers Versus Single PD Atoms at Different Anatase Facets

Rybakov, Andrey A.; Larin, Alexander V.; Vercauteren, Daniel P.; Todorova, Silviya

Link to publication

Article

Higher Catalytic Activity of Pd Monolayers Versus Single PD Atoms at Different Anatase Facets

Andrey A. Rybakov [1], Alexander V. Larin [1] , Daniel P. Vercauteren [2,*] and Silviya Todorova [3,*]

1. Department of Chemistry, Moscow State University, GSP-2, Leninskie Gory, Moscow 119992, Russia; rybakovy@gmail.com (A.A.R.); nasgo@yandex.ru (A.V.L.)
2. Laboratory of Computational Physico-Chemistry, Namur Institute of Structured Matter, University of Namur, Rue de Bruxelles 61, B-5000 Namur, Belgium
3. Institute of Catalysis, Bulgarian Academy of Sciences, Acad. G. Bonchev St., Bldg 11, 1113 Sofia, Bulgaria
* Correspondence: daniel.vercauteren@unamur.be (D.P.V.); todorova@ic.bas.bg (S.T.)

Abstract: The structure and catalytic activity of Pd monolayers versus single Pd atoms were studied for the reverse water–gas shift reaction (rWGSR) at the anatase (101) and (001) facets for which Pd flat fragments have been observed experimentally. Thermodynamic and partial kinetic analyses of five steps of the rWGSR scheme were considered on the two facets. The projected density of states for the d-orbitals of single Pd atoms of the (101) facet of a-TiO$_2$ are compared to the ones for Pd atoms in both monolayers at (101) and (001) facets to interpret the different activity of Pd. The low activity of single Pd atoms is probably related to the (001) facet, while a Pd monolayer participates at the (101) facet due to its heterogeneity induced by the support.

Keywords: reverse water–gas shift reaction; flat cluster; density of d-states

1. Introduction

The significance of "peripheral" metal atoms at the "nanoparticle-support" interfaces has been demonstrated for the kinetics of various chemical processes, emphasizing the need to understand the catalytic role of all interface atoms in contact with the support [1–3]. The maximal effect could correspond to an "open" contact monolayer or small flat clusters, which serve as a necessary reaction media for water–gas shift reactions (WGSR) [4], while the nearest atoms of the support around the cluster come into play mainly for the kinetic schemes [5]. The participation of small flat metals Me$_n$ clusters up to n = 16 atoms, Me = Pd, Pt, Au, and Ni has already been studied experimentally in details for Ni/TiC in the reverse WGSR (rWGSR) [4,5] and for carbides and nitrides for the WGSR [6,7]. Regarding Me deposition on oxides, Rh [8,9] and Pt [10,11] monolayers on Al$_2$O$_3$, flat clusters, such as Ir$_n$/MgO, n = 4, 6 [12], Ru$_6$/MgO, Ru$_6$/TiO$_2$, Ru$_{12}$/SiO$_2$, Ru$_6$/Al$_2$O$_3$ [13], Rh/TiO$_2$ [14], and Ni/WC [15], have been extensively studied. Particularly, a more defective rutile TiO$_2$ polymorph was often used as support. Quasi-two-dimensional Au and Pd clusters were observed on the rutile (110) facet [16], and the catalytic activity of a Pd$_{28}$ monolayer on its (001) facet for water dissociation has been shown with a barrier of 0.69 eV [17]. New surface states in a Pd slab were discussed at TiO$_2$ [18,19], while a non-metallic state of deposited Au was also observed [20].

Recently, the formation of a monolayer or a bilayer of Pd flat fragments from single Pd atoms on the anatase (101) facet (~90% of total anatase surface) upon H$_2$ pressure has been observed experimentally in correlation with the highest reaction rate of rWGSR [21]. An H$_2$ atmosphere was used earlier for obtaining flat Ru$_{12}$ clusters at SiO$_2$ and Ru$_6$ at TiO$_2$ following the reaction between supports and Ru$_3$(CO)$_{12}$ [13]. Both Ru$_{12}$ and Ru$_6$ clusters showed a higher activity for CO hydrogenation [14]. In the first parts of the present work, we estimated the stability of anatase facets (Section 2.1) and formulated an rWGSR scheme (Section 2.2). Then, we attempted to interpret the experimental geometry from

EXAFS data for different positions of single Pd atoms (Fresh model [21]) to allow the possibility of reaction's analyses (Section 2.3), their reactivity towards H_2 (Section 2.4), a crucial step for single Pd atoms for WGSR, at least at the main (101) facet. After obtaining monolayer models, their geometries were also compared to EXAFS geometries related to the experimental H400 model that shows the presence of flat Pd species obtained in an H_2 atmosphere (Section 2.5) [21]. The thermodynamics of a five-step rWGSR scheme have been calculated at selected single Pd and two monolayer models (Section 2.6). Kinetic analyses were applied to the most probable variants of rWGSR at (101)a-$Ti_{16}O_{32}$ (Section 2.6.3). The densities of d(Pd) orbitals were analyzed to reveal their correlations with Bader charges and catalytic activity (Section 2.7). Comparison with the properties of Pd monolayers from the literature is presented in Conclusions (Section 5).

2. Results

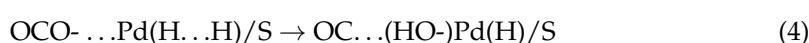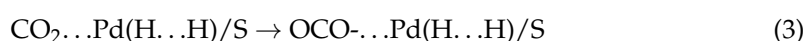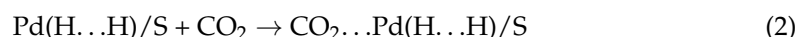### 2.1. Relative Stability of the Different Anatase Facets

Regarding the dominant (101) facet (up to 90%) of anatase, we admitted that the remaining 10% of the surface represented by less stable facets like (001) could also be important at small Pd coverage (0.0125 wt.% Pd), as studied in ref. [21]. Despite the TiO_2 supercell used for the (101) slab being smaller, it turns out to be more stable than the (001) slab in terms of surface energy: $\gamma = 116$ meV/$Å^2$ for (101)$Ti_{16}O_{32}$ versus 145 meV/$Å^2$ for (001)$Ti_{27}O_{54}$), or, in terms of energy per TiO_2 unit, $E_{TiO2} = -26.856$ eV/(101)TiO_2 versus -26.734 eV/(001)TiO_2. It is worth mentioning that the Pd stabilization at the less stable (001) facet (loss of energy of -23.9% and -1.3% only relative to that for Pd bulk) is better (Table 1) than at the (101) one (-41.1% and -43.5%). This deeper Pd stabilization at the less stable (001) facet provides additional evidence that the expansion of the facets for a possible Pd location would be reasonable.

Table 1. Pd stabilization $\Delta U_{Pd}/U_{Pd}$ ($\Delta U_{Pd} = U - U_0$, all in eV), where U_0 is the energy of the empty cell, relative to the one for Pd bulk ($U_{Pd} = 5.838$ eV, as obtained at the PBE-D3/PAW level) for the adsorption of one Pd atom at the A or B sites, of (101) and (001) facets.

hkl	Site	$-U$	$\Delta U_{Pd}/U_{Pd}$, %
101	A	433.227	−41.1
	B	433.049	−43.5
	U_0	429.789	-
001	A	876.471	−23.9
	B	877.792	−1.3
	U_0	872.028	-

2.2. rWGSR Scheme

From a chemical point of view, it is instructive to understand the reasons for the lower activity of single Pd atoms (Fresh model [21]) compared to the flat Pd fragments obtained experimentally (H400 model [21])) for the rWGSR scheme. Our modeling here is constrained primarily by thermodynamic analysis of the rWGS chain of reactions with the Pd species on the support S = a-TiO_2 when the system was initially treated by H_2:

$$Pd/S + H_2 \rightarrow Pd(H...H)/S \tag{1}$$

$$Pd(H...H)/S + CO_2 \rightarrow CO_2...Pd(H...H)/S \tag{2}$$

$$CO_2...Pd(H...H)/S \rightarrow OCO-...Pd(H...H)/S \tag{3}$$

$$OCO-...Pd(H...H)/S \rightarrow OC...(HO-)Pd(H)/S \tag{4}$$

$$OC...(HO-)Pd(H)/S \rightarrow OC...(H_2O)Pd/S \tag{5}$$

At the thermodynamic level, we shall see that some steps can be discriminated and deleted at the initial steps to avoid the time-consuming search of transition states. In order

to reliably clarify the reactivity, the known structural parameters must be reproduced in the calculations as closely as possible, starting from single Pd atoms.

2.3. Interpretation of Single Pd Positions at (101) and (001) Facets Versus Experiment

Two Pd sites (1Pd_A and 1Pd_B in Table 2) were tested at the (101) facet for comparison with the experimental EXAFS geometries (Pd coordination number N_X and Pd-X distances relative X atoms [21]), which are known as the initial "Fresh" state of the reagent, confirmed as single atoms at the facet being the most stable. According to the Fresh model [21], three O atoms should be in the first coordination sphere (around 2.0 Å), one Ti atom (2.95 Å) is in the next layer, and seven more O atoms at 3.78 Å [21]. However, the favored 1Pd_A site at (101) (Figure 1a) possesses four Ti atoms in the second sphere (2.840, 2.845, 2.881, 2.884 Å) instead of one (2.95 Å). The less stable 1Pd_B site at (101) (Figure 1c) has two O atoms in the first shell (2.128, 2.162 Å), one Ti in the second one, which is too close to Pd (2.528 Å instead of 2.95 Å), and two O atoms in the third one (3.135, 3.160 Å). So, both Pd positions at (101) are not ideal as a confirmation of the experimental Fresh model [21]. This is the reason we tested the less stable (001) facet, whose fraction of 10% can provide an important contribution to the EXAFS signals from Pd positions, especially at a low Pd coverage of 0.0125 wt.% Pd for the Fresh model [21]. The second additional argument in favor of the less stable facet is that its activity is usually higher, as shown for CH_4 dissociation on different PdO facets, irrespective of the oxide support for PdO [22]. One can see below that it is valid for the systems under study, i.e., Pd is better stabilized at the less stable (001) facet (Table 1).
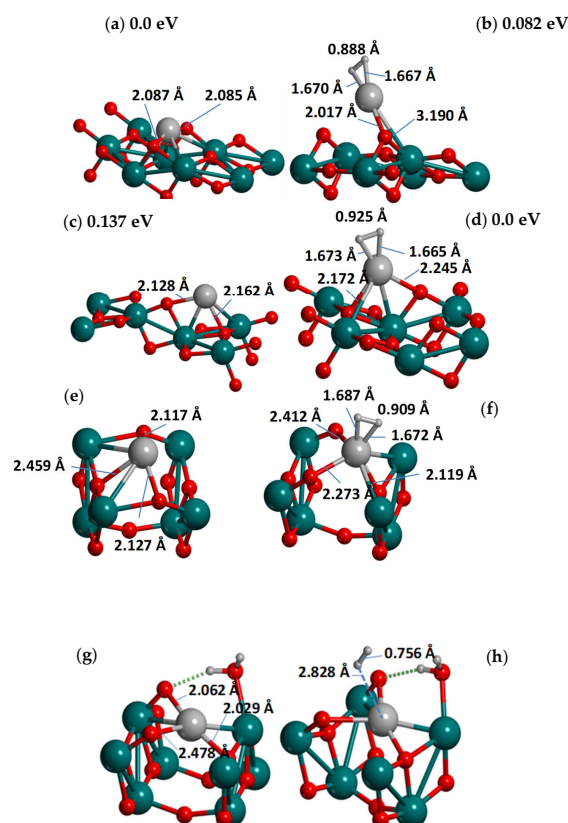
Figure 1. Initial (**a,c,e,g**) Pd positions and (**b,d,f,h**) positions after adsorption of the H_2 molecule optimized at (**a–d**) (101)a-TiO$_2$ or (**e–h**) (001)a-TiO$_2$. Relative energies are shown separately for the (**a,c**) and (**b,d**) groups. Pd-O distances of the first coordination Pd sphere are shown in Å. Atomic colors are gray (small), red, cyan, and gray (large) for H, O, Ti, and Pd. The lower oxide part is omitted for clarity. The Pd-O distances are also given in Table 2.

Table 2. |Pd-X| distances (X = Pd, O, Ti), as calculated on the (101) and (001) anatase facets and obtained at the PBE-D3/PAW level, in comparison with the experimental EXAFS data (coordination number N_X and distances from ref. [21]), related to the different treatments and conditions at loading 0.0125 wt.% Pd (Fresh for single Pd atoms, H400 for flat Pd clusters). Theoretical models are 1Pd_Y atoms for single Pd atoms, N = A, B, and 12Pd ($Pd_{12}/a-TiO_2(101)$) or 18Pd ($Pd_{18}/a-TiO_2(001)$) for flat Pd clusters. Relative stabilities of the 1Pd_Y models (for single Pd atoms) or numbers of atoms M (format PdM) of the same Pd monolayer are given in the third column.

Case	Y	−U/PdM	No	|Pd − O|, Å	N_X	|Pd − X|, Å
101	A	0.000	3	2.085, 2.087, 2.606	4	2.840, 2.845, 2.881, 2.884, X = Ti
			7	3.409, 3.412, 3.535, 3.535, 3.535, 4.534, 4.529		
	B	0.137	2/2	2.128, 2.162/3.135, 3.160	1	2.528, X = Ti
			7	3.135, 3.160, 3.979, 4.014, 4.272, 4.239, 4.296		
001	A	0.321	3	2.115, 2.127, 2.459	2	2.981, 2.956, X = Ti
			7	3.005, 4.061, 4.077, 4.223, 4.241, 4.401, 4.410		
	B	0.000	2	2.014, 2.102	2	2.344, 2.991, X = Ti
			8	2.808, 2.993, 3.376, 3.377, 3.464, 3.743, 3.746, 4.032		
	B [a]	−0.762	3	2.029, 2.062, 2.478	2	2.368, 2.882, X = Ti
			7	2.920, 2.937, 3.403, 3.455, 3.469, 4.041, 4.110		
Fresh [b]		-	3.2 ± 0.4	2.00 ± 0.01	1.2 ± 0.3	2.95 ± 0.03, X = Ti
			7 ± 0.2	3.87 ± 0.03		
101	12Pd	Pd50	1	2.082	5	2.768, **2.774** [c], **2.573**, 2.561, 2.739, X = Pd
					2	3.831, 3.727, X = Pd
		Pd59	1	2.187	6	2.728, **2.779**, 2.667, 2.715, 2.774, **2.633**, X = Pd
001	18Pd	Pd114	1	1.999	5	**2.919**, 2.723, 2.765, 2.805, **2.716**, X = Pd
					2	3.746, 3.947, X = Pd
		Pd110	1	2.104	5	**2.703**, 2.766, 2.814, 2.807, **2.829**, X = Pd
					2	3.833, 3.932, X = Pd
H400 [b]		-	0.4	2.13 ± 0.04	6.8 ± 0.6	2.761 ± 0.006, X = Pd
			2.7 ± 0.3	2.533 ± 0.007	1.6 ± 0.4	3.83 ± 0.02, X = Pd

[a] hydrated 1PdOH_B site, U_{H2O} = −14.27 eV; [b] experiment from ref. [21]; [c] values given in bold show the minimal and maximal distances to the X atom when it is relevant.

At the (001) facet, both 1Pd_A (Figure 1e) and 1Pd_B sites deviate from the ideal agreement with the experimental Fresh model [21] (Table 2), but the less favorable 1Pd_A presents a better coincidence, as it has three closest O neighbors instead of two O for 1Pd_B. We tried to modify the last 1Pd_B site using water adsorption nearby so that it resulted in three closest O neighbors (Figure 1g). Such adsorption (and/or following water

dissociation) conserves the Pd 3-coordination in the first shell like in the experimental Fresh model with 1PdOH_B, but its second shell also contains a Ti atom, which is too close (2.368 Å) to Pd compared to the experiment (2.950 Å). It is interesting to note that the 3-coordinated Pd (the first coordination shell) remains unchanged regardless of whether adsorbed water (Figure 1h) is dissociated. A more detailed discussion of the experimental data is presented in Discussion (Section 3.3).

2.4. H_2 at Single Pd Atoms of (101) and (001) Facets

The presence of 2- and 3-coordinated O atoms at the (001) and (101) facets, respectively, causes a drastic difference relative to H_2 dissociation on a single Pd atom. A higher 3-coordination of oxygens at (101) results in a problematic energy gain upon dissociation of H_2 with poor coordination of H atoms. It confirms a higher endo-thermic effect relative to the products at 1Pd_A site with H atoms trapped by two O (1.957 eV) versus those at Pd and O sites (1.396 eV). The rWGSR channel for single 1Pd_A atom at (101) is thus forbidden due to the high endothermic effect of H_2 dissociation. The 1Pd_B site is even less coordinated to the support, resulting in a longer H...H distortion of 0.925 Å versus 0.889 Å for 1Pd_A (Figure 1a,c) that should result in even a higher endothermic effect of H_2 dissociation than for 1Pd_A.

Two single 1Pd_A and 1PdOH_B sites at (001) could be involved in rWGSR because less saturated 2-coordinated O atoms at the (001) facet lead to exothermic heat of H_2 dissociation at 1Pd_A (−0.479 eV) or a hydrated model of 1PdOH_B (−0.117 eV) single atom (Table 3). The higher energy of H_2 adsorption at 1Pd_A (−1.337 eV versus −0.761 eV at 1PdOH_B Table 3) agrees with the better stabilization of 1PdOH_B (the shorter Pd-O bond lengths in Table 2). The difference between the 1Pd_A (Figure 1f) and 1PdOH_B (Figure 1h) corresponds to the chemisorbed state (|H-H| = 0.909 Å, Figure 1f) and physisorbed states (|H-H| = 0.756 Å, Figure 1h) of H_2. As a reminder, the optimized H-H distance in the gas state is 0.7503 Å at the PBE/PAW level, which is short relative to the accurate and theoretical equilibrium value of 0.7667 Å [23]. Despite the fact that the initial model of the hydrated 1PdOH_B model was simplified after H_2 dissociation, i.e., water was desorbed between steps, Figure S2b,c, the main problem of this model occurs at the last step (Figure S2f). In the final product, dissociated water is essentially more stable, thus hindering H_2O desorption before a new catalytic cycle. Using accepted notations, case (f) for hydrated 1PdOH_B in Table 3 corresponds to dissociated H_2O while the recombination is strongly hindered.

Table 3. Energy variations ΔU_X of the different processes (X = ads for adsorption, X = dis for dissociation, X = rea for reaction leading to the products in the current line) on (101) and (001) facets of anatase with participation of single atoms (1Pd_A or 1PdOH_B with adsorbed water) and monolayers (12Pd, 18Pd) as obtained at the PBE-D3/PAW level. The N index (second column) corresponds to the order in Figure 2 (Pd$_{12}$/(101)a-TiO$_2$) or Figure 3 (Pd$_{18}$/(001)a-TiO$_2$).

X	N	Product	(101)		(001)		
			1Pd_A	12Pd	1Pd_A	1PdOH_B	18Pd
ads	(a)	H_2	−0.727	- [f]	−1.337	−0.761 [a]	−1.042
dis	(b)	H...H	1.957 [d], 1.396 [e]	−1.646	−0.479 [d], 0.248 [e]	−0.117 [a]	−0.332
ads	(c)	H...H...CO$_2$	-	−0.588	−0.222, −0.277	0.0 [b]	0.280
rea	(d)	H...H...OCO$^-$	-	−0.307	−0.258	−0.315	−0.512
rea	(e)	CO + OH$^-$	-	−0.594	−1.088	0.712 [c]	−1.058
rea	(f)	CO + H$_2$O	-	−0.186	−1.271	−3.083 [g]	0.244

[a] hydrated form; water is desorbed before CO$_2$ adsorption; [b] no heat of CO$_2$ adsorption can be estimated due to dehydration at previous stage and the necessity to know the heat of dehydration, it is close to that in the same row on the left (−0.222 eV) for the 1Pd_A model; [c] HOCO is formed compared to separate Pd-CO and Pd-OH groups; [d] H-O and H-O products; [e] H-O and H-Pd products; [f] no chemi- or physisorbed H$_2$ can be optimized, dissociation occurs unhindered; [g] the geometries for (a–f) steps for 1PdOH_B models are shown in Figure S2a–f.
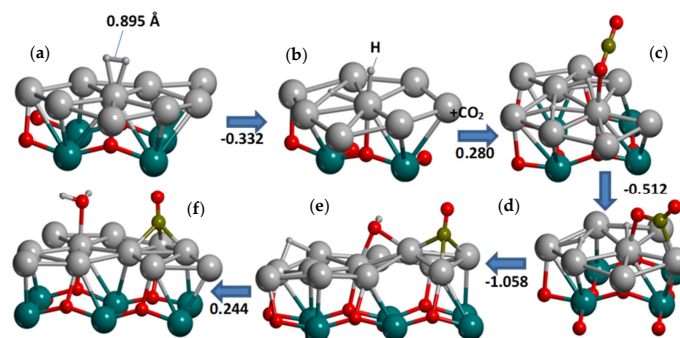
Figure 2. rWGSR steps (1–5) on Pd_{18} layer at (001)a-TiO_2. Atom colors are gray (small), olive, red, cyan, and gray (large) for H, C, O, Ti, and Pd. The lower oxide part and part of Pd atoms are omitted for clarity. The (**a**–**f**) configurations are commented in Table 3. Heats of the reactions (eV) are noted near arrows.
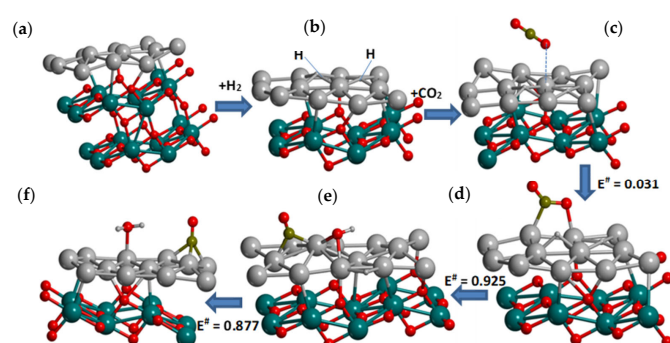

Figure 3. rWGSR steps (1–5) on Pd12 layer at (101)a-TiO_2 (one complete unit cell altogether in (**a**) view). Atomic colors are gray (small), olive, red, cyan, and gray (large) for H, C, O, Ti, and Pd. The lower oxide part is omitted (except (**a**)). No H_2 adsorbed is shown in (**a**), see Table 2 (H_2 dissociation occurs unhindered). The (**b**–**f**) configurations are commented in Table 3. Barriers $E^{\#}$ of the steps (3–5) are noted below arrows (eV).

2.5. Models of Pd Monolayers at (101) and (001) Facets

The knowledge about formation of flat Pd fragments on anatase [21] allows verifying whether or not larger flat fragments can be stabilized. The limiting case for such deposition corresponds to a periodic monolayer with a period defined by the support as already observed in the literature for carbides [24,25], alumina [26], and rutile [17]. Changing different geometries of initial (100)Pd monolayers at the (101)TiO_2 surface, we proceeded to approximate Pd densities in other monolayers as already optimized for other oxides [17,26]. Optimizing the n-value in various models of the (001)Pd_n monolayer relative to the (101)TiO_2 surface, we succeeded in obtaining the "1/2" model (Figure 4a), where the values in "N/M" notation correspond to the numbers of alternate bands of squares and triangles associated with (100) and (111) facets. A (1/2)Pd_{12}/cell monolayer was obtained at a density of 6.458 $Å^{-2}$, which is intermediate between the previous densities of 6.292 $Å^{-2}$ for alumina [26] and 6.761 $Å^{-2}$ for rutile [17]. An analogous 1/4 (Figure 4c) form has already been obtained at the (100)γ-Al_2O_3 [26].

At the (001)TiO2 surface, a (9–9)Pd_{18}/cell monolayer was obtained with a lower Pd concentration of 7.161 $Å^{-2}$. The "9–9" notation corresponds to two 9-atom squares (squares in Figure 4c) per unit cell. Such a coordination within a monolayer has been previously modeled in the gas phase for Au_9Pt_9 per UC with alternate Au_9 and Pt_9 squares [27].

Pd atoms are charged both positively and negatively (Table 4) due to the contact with different atoms of the support, resulting in a non-zero total Bader charge Q of the monolayer. Different contacts at the (101) and (001) facets led to positive (0.240 e) and negative (−0.547 e) total slab charges Q (Table 4). The extent of the atomic charge variations is expressed as $\Delta Q = Q_{max}(Pd) - Q_{min}(Pd)$, where Q_{max} and Q_{min} are the maximum and

minimum Pd charges in the cell. The charge gap ΔQ is similar for both slabs. Regarding the higher activity of Pd with positive charges at alumina [26] and rutile [17], we analyzed routes (1–5), starting at atoms with positive charges.
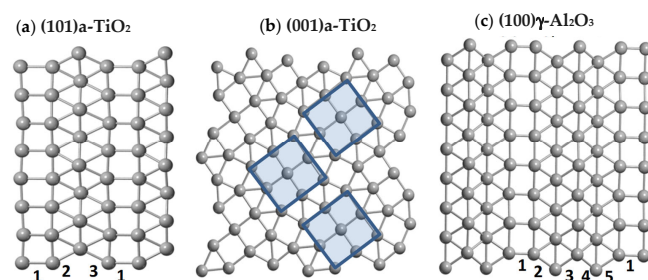

(a) (101)a-TiO₂ (b) (001)a-TiO₂ (c) (100)γ-Al₂O₃

Figure 4. Examples of 2 × 2 unit cells of "1/2" (**a**), "9–9" (**b**), and "1/4" (**c**) models as optimized at the PBE-D3/PAW level at (101)a-TiO$_2$, (001)a-TiO$_2$, (100)γ-Al$_2$O$_3$ [26] with 12, 18, and 20 Pd atoms per unit cell. Values in "N/M" notations (**a,c**) correspond to the numbers of alternate (100) and (111) type vertical bands (shown below cases (**a,c**)). The "9–9" notation corresponds to two 9-atom squares (shown by squares in (**b**)) per unit cell.

Table 4. Bader charges for Pd atoms, the charge gap $\Delta Q = Q_{max}(Pd) - Q_{min}(Pd)$, Q_{max} and Q_{min} being the maximum and minimum Pd charges (shown in bold), the total charge Q of Pd monolayers with 18 and 12 atoms per cell at (001) and (101) facets of a-TiO$_2$, respectively, optimized at the PBE-D3/PAW level.

N	(001)	N	(101)
100	0.114		
101	−**0.208**		
102	0.117		
103	−0.166	49	0.062
104	**0.163**	50	0.190
105	−0.125	51	−0.033
106	0.074	52	−0.123
107	−0.168	53	**0.173**
108	0.142	54	−0.116
109	−0.173	55	−**0.145**
110	−0.038	56	0.156
111	−0.193	57	−0.023
112	0.124	58	−0.026
113	−0.160	59	0.120
114	0.149	60	0.005
115	−0.117		
116	0.083		
117	−0.165		
Q	−0.547	Q	0.240
ΔQ	0.371	ΔQ	0.318

2.6. Reactivity of Monolayer at (101) Facet

2.6.1. Hydrogen

High reactivity of the Pd$_{12}$ monolayer towards H$_2$ could be explained regarding a strongly chemisorbed H$_2$ state at separate Pd atoms with very long |H-H| distances (~0.8 Å or even more in Figure 1c,d compared to gas state value |H-H| = 0.7503 Å, obtained at the PBE/PAW level). It is important that all H atoms remain bonded to Pd after dissociation rather than to the support. Hence, one proposes a small activation energy of H$_2$ dissociation at the Pd12 monolayer as well as for close Pd atoms.

The heterogeneity of Pd monolayer (Table 4) is important for the selection of the H$_2$ adsorption site. The variation of different initial H$_2$ geometries at the Pd50 atom with a positive atomic charge 0.19 |e| (Table 4) led to an easy dissociation and does not allow the obtaining of non-dissociated H$_2$. Selecting the Pd$_{54}$ atom with negative charge −0.116 |e| resulted in physisorption (Table 4). Strong chemisorption at positive Pd$_{50}$ and weak H$_2$ adsorption at negative Pd$_{54}$ are similar to the drastic variation in the heats

of adsorption of H_2O and NH_3 at alumina (Figure 4 from ref. [26]). The heats of their adsorption at Pd sites with positive and negative charges within some Pd monolayers differ up to two times [26].

2.6.2. CO_2 to Carboxylate

The activity of the Pd monolayers versus H_2 dissociation exceeds the one noted for single Pd atoms at one anatase facet. This favors the initial stage of rWGSR when H_2 seems to be a barrierless process. In the (2–3) stages, CO_2 conversion to carboxylate is required. The question about the concurrence between the already dissociated H atom and CO_2 was also considered at (001)a-TiO_2 via CO_2 adsorption at one Pd atom (Figure 2c), occupied by an atop H (Figure 2b), which was shared with the neighboring Pd after adsorption (Figure 2c). Energy loss is around 0.280 eV at (001)a-TiO_2, while CO_2 adsorption at free "positive" Pd of (101)a-TiO_2 (Figure 2b) results in a gain of -0.588 eV (Table 3, Figure 3c). The Pd atom at (101)a-TiO_2 (Figure 3b) shared two H atoms which are both 4-coordinated so that the energy loss at (001)a-TiO_2 is partly related to the H-transfer from atop to a 4-coordinated site (or hole site).

A drastic difference has been observed between the OCO- carboxylate formation from CO_2 at a single Pd atom and the Pd_{12} monolayer. In the first case, the activation energy $E^{\#}$ exceeds 0.7 eV, while the barrier disappears at the Pd_{12} monolayer. The main $E^{\#}$ part is the change of the adsorption energy of CO_2 (between reaction coordinate points 0 and 1 in Figure 5) which corresponds to a rotation, and steeply approaches the transition state (TS at point 5 of Figure 5) at a single Pd. The minor difference between points 1 and 4 is the energy change due to CO_2 rotation at nearly the same distance Pd...C. The slight increase in energy between points 4 and 5 (TS) is due to the shortening of the Pd...C distance from 3.453 to 2.937 Å (the O-C-O angle changes by 4° only). For comparison, CO_2 dissociation at (110)Ni is preceded by a similar surface diffusion with a barrier of 0.44 eV in the absence of the significant role of important electrostatic contributions with rotation [28].
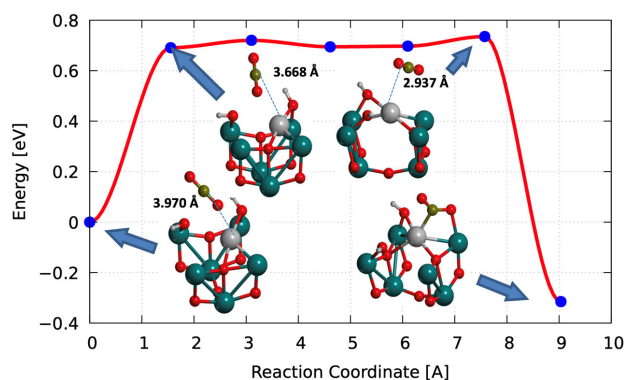

Figure 5. Reaction profile of carboxylate formation for the 1PdOH_B model of a single Pd atom. Pd...C distances (dashed or solid lines) are shown in Å for the different steps. Atomic colors are gray (small), red, cyan, and gray (large) for H, O, Ti, and Pd. The lower part of oxide atoms is omitted for clarity.

2.6.3. Comparison Between (3–5) rWGSR Stages of at (101) and (001) Facets

The calculated activation energies show as a limiting stage of the carboxylate reaction with H (4), with the appearance of CO and OH at Pd_{12}/(101)a-TiO_2. Stage (4) splits into two stages with the formation of HOCO species (Figure 6c). The respective maximal barrier value of 0.925 eV for step (4b) (Table 5) is less than the experimental 1.2 eV value [21]. This barrier is larger than the activation energy of step (5), which is 0.877 eV. As noted below (Section 3.1), H_2O recombination is generally an endothermic process at different Pd monolayers [17,26], but in the present case one observes a slight exothermic reaction (-0.186 eV in Table 3, Figure 3f). This effect is explained by a parallel stabilization of

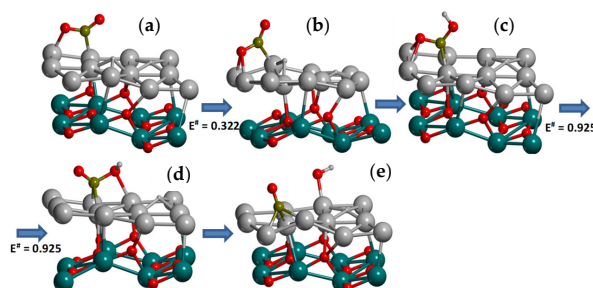the deformed monolayer at step (5) (between Figure 3e,f), which compensates for the energy loss.

Figure 6. Reagent (**a**), transition states (**b**,**d**), intermediate (**c**), and product (**e**) of the 2-step rWGSR stage (4) at (101)a-TiO$_2$ with Pd$_{12}$ layer. Atomic colors are gray (small), olive, red, cyan, and gray (large) for H, C, O, Ti, and Pd. The lower oxide part is omitted for clarity. The steps are commented in Tables 4 and 5. Barriers E$^\#$ of steps (4a, 4b) are noted below the arrows (eV).

Table 5. Energy variations of ΔU and barriers E$^\#$ (both in eV) along reaction steps (3–5) at Pd$_{12}$/(101)a-TiO$_2$ as obtained at the PBE-D3/PAW level. Geometries are given in Figure 6.

Step	ΔU	E$^\#$
(3)	-0.303	0.031
(4a)	-0.174	0.322
(4b)	-0.598	0.925
(5)	0.140	0.877

Encountering problems for accurate modeling with the barrier for step (5) at Pd$_{18}$/(001)a-TiO$_2$, we paid attention to the nearly invariant position of 3-coordinated CO during the last step (5) (between Figure 3e,f) at the (001)a-TiO$_2$ in contrast to the strong reconstruction of the Pd$_{12}$ at (101)a-TiO$_2$ noted above in step (5). The reaction thus corresponds to a water recombination with an endothermic heat of 0.244 eV (Table 3). Therefore, we calculated a cNEB profile (Figure 7b) for the H$_2$O dissociation reaction at the pristine Pd$_{18}$/(001)a-TiO$_2$ facet without pre-adsorbed CO$_2$. The final barrier corresponds to an inverse reaction in Figure 7b. It leads to a barrier of 0.960 eV (Figure 7b) close to 0.877 eV for (101) facet (Figure 7a) with low imaginary TS frequency of 290i cm^{-1}. The reaction involves Pd vibrations together with O-H elongation that explains the low TS frequency associated with H transfer.
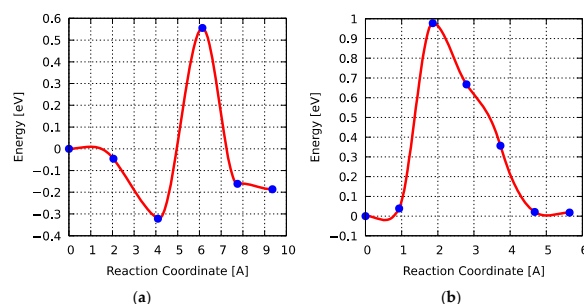

Figure 7. Reaction cNEB profiles of (**a**) step (5) at Pd12/(101)a-TiO$_2$ and (**b**) water dissociation at Pd18/(001)a-TiO$_2$ at the PBE-D3/PAW level.

2.7. pDOS and Pd Charges at Different Pd Coordinations

The question of a proper descriptor for the reactivity of d-metals has been often discussed in the literature, wherein surface core level shift, peak of the center of the d-zone, and CO chemisorption [29] have been critically analyzed [30–32]. Herein we verified the behavior of the intensities of the d(Pd) density below the Fermi level. Projected density of states (pDOS) for the Pd d-orbitals at the (a) A and (b) B sites of the (101) a-TiO$_2$ reflects

different coordination of Pd atoms at both sites (Table 2). This can be illustrated via comparison of densities of the d(Pd) orbitals, which increase by up to double from site A (Figure 8a) to the less coordinated site B (Figure 8b). It is also useful to compare the DOS of d(Pd) orbitals below the Fermi level (0 eV in Figure 8) with the ones for Pd in the monolayers below (Figure 9). It is done in Section 3.2 with the Bader charges.
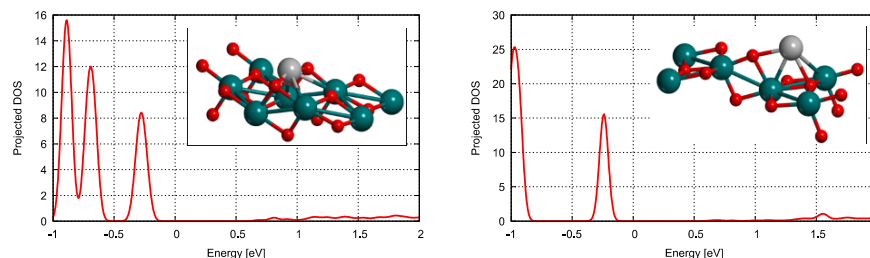

Figure 8. Projected density of states (pDOS) for the Pd d-orbitals at the (**a**) A and (**b**) B sites of the (101) facet of a-TiO$_2$. The relative energy is given in eV, and details of the geometries are given in Table 2. A different density scale (along OY) is applied in (**a**,**b**). Atomic colors are gray (small), red, cyan, and gray (large) for H, O, Ti, and Pd. Spin non-polarized solutions are presented as a sum of α- and β-densities.
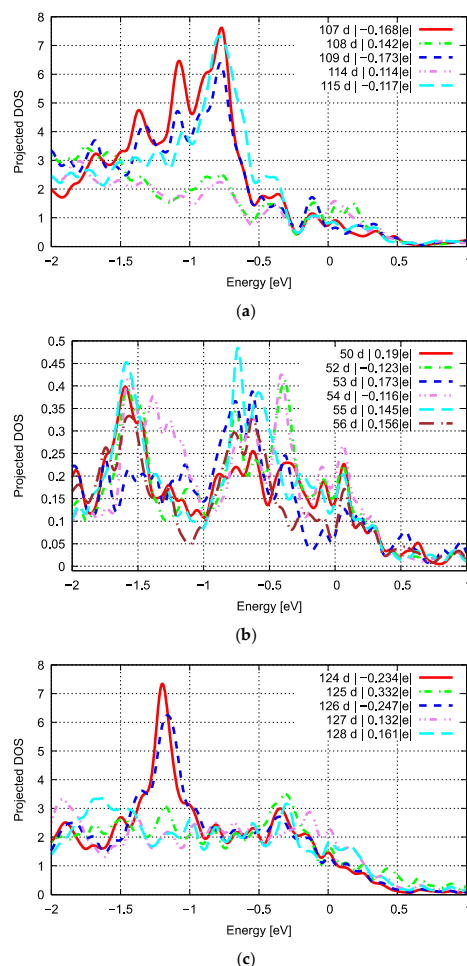

Figure 9. pDOS of d(Pd) orbitals for Pd with positive and negative Bader charges (|e|), being part of monolayers deposited at (**a**) (001)-aTiO$_2$, (**b**) (101)-aTiO$_2$, and (**c**) (100)γ-Al$_2$O$_3$ [26]. Spin (**a**,**c**) non-polarized and (**b**) polarized (α only) solution is given so that the absolute values in (**b**) should be multiplied by 2 for comparison.

3. Discussion

3.1. H_2O Recombination at Other Pd Mononolayers

Water dissociation at the $Pd_{18}/(100)\gamma$-Al2O3 (with vacancies in the monolayer) and $Pd_{20}/(100)\gamma-Al_2O_3$ (Figure 4c) monolayers [26] and $Pd_{28}/(001)$rutile-TiO_2 (with one divacancy in the monolayer) [17] has already been studied by us, with mentioning of activation barriers and heats of the reaction for recombination as well. In all these systems, recombination (last step (5)) is also endothermic, with barriers ranging from 0.68–1.07, 0.58 [26], and 0.78 eV [17], respectively. The interval of barriers for $Pd_{18}/(100) \gamma - Al_2O_3$, 0.68–1.07 eV, comes from the heterogeneity of the Pd monolayers. The most active sites, at least from those already studied for the other supports, possess recombination barriers below 0.877 eV obtained herein. Analogous dissociation barriers are lower, i.e., 0.37–0.67, 0.40 [26], and 0.69 eV [17], respectively. It signifies that Pd monolayers are better suited for direct WGSR where water dissociation is required at the first step.

3.2. Density of States for Pd Atoms and Monolayers over Different Supports

It is instructive to compare the pDOS of d(Pd) for different systems, including literature data from refs. [17,24–26]. The absolute values of DOS of d(Pd) per atom are comparable to those calculated for bulk Pd (~1.3 states/eV), Pd(111) facets (~1.5 states/eV), and Pd slabs at TiC(001) (<0.5 states/eV) below and close to the Fermi energy [24]. In the same interval (-0.5, 0.0), the d(Pd) maximum is much larger for single Pd than for bulk Pd or Pd(111) facets, decreasing with higher coordination from ~15 states/eV for 1Pd_A/(101) to ~8 states/eV for 1Pd_A/(101) (Figure 8). To compare the spin non-polarized solution data from Figure 8 with literature data, one should divide them by 2, obtaining ~7.5 states/eV for 1Pd_B/(101) to ~4 states/eV for 1Pd_A/(101) atom. Smaller d(Pd) values per one atom can be found for Pd monolayer at TiC [25], where total d(Pd) for a unit cell with 4 Pd atoms has similar maximum ~7 states/eV for spin non-polarized solution (α- or β-density) in Figure 2b from ref. [25]. It yields 7/4 ~ 1.7 states/eV per one atom. High density of states below the Fermi level is one of the reasons why transition metal carbides have become the objects for metal deposition for catalysis. A single Pd atom has a higher d(Pd) per atom below and close to the Fermi level (Table 6, Figure 8) than the ones calculated herein (Figure 9) or in the literature [17,24–26], but the advantage of a single Pd only applies to some reactions that do not require a specific arrangement for reagents.

Table 6. Bader charges Q_B ($|e|$), projected density of states for d-orbitals Pd and monolayers (d(Pd), states/eV), respective position E (eV) at the various supports. d(Pd) per atom from spin non-polarized values are obtained from Figure 1a,c, 5 by dividing per 2.

System	Q_B, $\lvert e \rvert$	d(Pd)	E
$Pd_{18}/(100)\gamma$-Al_2O_3	0.132	1.4	−0.17
	0.161	1.6	−0.30
	0.332	1.8	−0.30
$Pd_{18}/(001)$a-TiO_2	0.114	0.6	−0.12
	0.142	0.8	−0.12
$Pd_{12}/(101)$a-TiO_2	0.145	0.18	−0.26
	0.190	0.20	−0.18
1Pd_A/(101)a-TiO_2		4.1	−0.27
1Pd_B/(101)a-TiO_2		7.5	−0.27
Pd_4/TiC [a]	-	0.4	−0.38
Pd_4/TiC [b]	-	1.5	-

[a] From Figure 3b of ref. [24]; [b] From Figure 2b of ref. [25], total α-DOS of the maximum below Fermi level is divided per 4 for spin polarized solution for Pd_4/TiC.

Observing similar d(Pd) values at TiC and oxides, one notes that similar Pd atomic densities correspond to all Pd atoms at TiC [24,25], while the densities are different between the Pd sites at each anatase facet or any oxide (Figure 9a–c). It opens the possibility to vary the d(Pd) difference between the atoms with required amplitudes which depend on the

facet and oxide. It is an alternative solution of metal activation compared to bi-metallic alloys, where regularity can hardly be achieved owing to segregation and disorder in the alloys of different metals.

In the previous part 3.1, it was mentioned that the recombination barrier calculated at $Pd_{12}/(101)a-TiO_2$ is the largest (0.877 eV) one compared to the values evaluated at the same computational level for alumina [26] and rutile [17]. Such difference could be assigned to the lowest d(Pd) values on $Pd_{12}/(101)a-TiO_2$ (Figure 9b) compared to the one on alumina (Figure 9c) or $Pd_{18}/(001)a-TiO_2$ (Figure 9a). The calculation of the barrier for the last system is in our hands and will demonstrate if our assumption is valid. It is also important to note that the largest d(Pd) values in the domain below and close to the Fermi level are related to negatively charged Pd atoms (Figure 9b), while for alumina d(Pd) of positively charged Pd atoms dominates (Figure 9c). An intermediate case is noted for $Pd_{18}/(001)a-TiO_2$ (Figure 9a). Earlier we noted that positive Pd charge is important for adsorption of H2O and NH$_3$ [26]. The coincidence of a positive Pd charge and its elevated d(Pd) density (despite of its lower total density) could have a stimulating effect for the reaction.

3.3. Geometries of Pd Species from Experiment and Computations

Differences between the experimental geometry and computational models are noted for both single Pd atoms, the Fresh model [21], and flat Pd species, the H400 model [21]. If one considers the total number of neighboring atoms in our computational models, then the agreement with the Fresh model is generally better than with H400. For the latter, none of the Pd atoms of two different monolayers at both (101) and (001) facets lead to a dense packing of Pd in H400 (Table 2) with the neighboring ones the O (at 2.13 Å), three O (at 2.533 Å), seven Pd (at 2.761 Å), and one or two Pd (at 3.83 Å) neighbors for flat Pd species. The extent of a coincidence with the Fresh model depends on the assumption of a higher dispersion of the third O-shell, around 3.87 Å compared to a very low one in experiment (0.03 Å). For example, the seventh O atom in the third shell of the 1Pd_A atom at the (101) facet is shifted up to 4.534 Å (Table 2). A similar proposition is justified to compare the calculated geometry with the H400 model. The dispersion of the third shell around 2.761 Å must be higher than the experimental one (0.006 Å) to reach the same number of the neighbors. The values within the third shell are closer to the experimental dispersion (within 2.919 Å) while a smaller number of atoms around, i.e., 8–9 in both our models against 11–12 in total from experiment are obtained (Table 2). The qualitative problem of our periodic model for flat Pd species is the absence of three O atoms at 2.533 Å found in the H400 model. These Pd...O distances can hardly be found in the monolayers obtained as a result of Pd oxidation (the Figure S1a with 3 oxygen atoms) or formation of OH groups at the $Pd_{12}/a-TiO_2(101)$ monolayer (Figure S1b with 3 OH groups). This explanation of the formation of oxidized Pd clusters seems to be less probable in H$_2$ media. The Pd-O distances in such a situation correspond to the first type of O atoms (2.0–2.13 Å in Table 2) but not to 2.533 Å. The possible reason of the O presence at 2.533 Å is that the flat Pd fragments at a-TiO$_2$(101) [21] are small and in contact with the surface O atoms of anatase; one such distance was found for both slabs at (101) and (001) corresponding to Pd...O pair with surface O atom. However, a realistic Pd position with three nearest O atoms separated by 2. 533 Å was obtained neither at (101), nor at (001) facets. An alternative explanation of the geometry deviation from experiment [13] is that the geometry for a Pd atom reproduced as H400 after EXAFS suits better to Pd in a deeper layer and not at the surface.

4. Materials and Methods

Computational Details

Unit cells of $(101)a-Ti_{16}O_{32}$ (7.569 Å, 10.239 Å, 20.305 Å, 111.69°, 90°, 90°) and (001)a-TiO2 (11.353 Å, 11.353 Å, 25.385 Å, 90°, 90°, 90°) with subsequent deposition of Pd monolayers were constructed using home-made software. Three different $Ti_{27}O_{54}$, $Ti_{36}O_{63}$ [22], and $Ti_{36}O_{72}$ models of a-TiO$_2$(001) were built which differ in the absence of Ti_9O_9 or O_9

layers. Total energies of the models were calculated at the PBE-D3 level with the VASP package [33,34]. The PBE functional [35] was combined with a plane wave basis set, the PAW pseudopotentials [36], as implemented in VASP [33,34]. The D3 semiempirical dispersion correction [37] was used whose accuracy for periodic systems has been shown to be comparable to that of D4 one [38]. The kinetic energy cut-off was imposed at 500 eV. No effect of temperature on the results was taken into account. The Brillouin zone sampling was restricted to the Γ-point for (001)a-TiO_2 and to $2 \times 1 \times 1$ for (101)a-$Ti_{16}O_{32}$. For the rWGS reaction steps, a climbing image nudged elastic band (cNEB) modeling [39] was applied at the PBE-D3 level.

5. Conclusions

The higher stability of the (101) facet makes the participation of active single Pd atoms in the reverse water–gas shift reaction more probable than for the (001) facet. Three-coordinated O atoms at the (101) facet lead however to highly endothermic H_2 dissociation at a single Pd, a drastic difference with a single Pd at the (001) facet where O atoms are 2-coordinated. A small but sufficient concentration of single atoms can be achieved with a small coverage at the less stable (001) one, which occurs less frequently. The moderate increase of (001) surface energy relative to the one for the (101) case suggests possible formation of (001). Two different "½" and "9–9" types of Pd monolayers were optimized at (101) and (001) facets with 12 and 18 Pd atoms per unit cell, respectively. The problematic dissociation of H_2 at a single Pd at the (101) facet is easily resolved at flat Pd species presented by any of two monolayers. For the most favored way of rWGSR at the (101) facet, the calculated activation energies lead to a limiting stage for the carboxylate reaction with an H atom (4) with the appearance of CO and OH. Stage (4) is split into two steps with the formation of HOCO species. A maximum barrier value of 0.877 eV is lower than the observed experimental value of 1.2 eV [21]. The relationship between Pd charges and highest DOS values below and close to Fermi level was analyzed including both H_2O recombination at the last step of rWGSR herein and H_2O dissociation at alumina and rutile obtained earlier. Higher d-DOS of positive Pd atoms is important for H_2O splitting and recombination. The d(Pd) decreases in the sequence $Pd_{18}/(100)\gamma$-Al_2O_3 > $Pd_{18}/(001)$a-TiO_2 > $Pd_{12}/(101)$a-TiO_2 with the increase of barrier of the recombination at the last step (5). In parallel, the d-DOS of positive Pd atoms overheads that of negative Pd atoms at $Pd_{20}/(100)$ γ-Al_2O_3, is comparable with that of negative Pd atoms at $Pd_{18}/(001)$a-TiO_2 and becomes smaller at $Pd_{12}/(101)$a-TiO_2. All Pd monolayers studied herein could be useful for direct WGSR when water dissociation is required at the first step because respective barriers are smaller than the ones for rWGSR.

A specific consequence of oxide's applications as supports is that Pd d-densities are different between the Pd sites of monolayer at each facet or oxide, while similar Pd atomic densities are noted for all Pd atoms of the monolayers at carbides. This gives the possibility to fit the d(Pd) difference between the atoms up to required amplitudes when the reaction can start. This could be a potential route for metal activation instead of preparing bi-metallic alloys for which a regularity of reactive sites can be hardly achieved (or limited by the natural case of a single atom alloy) owing to a disorder in the alloys with comparable fractions of the metals.

Author Contributions: A.A.R.: Visualization, Investigation, Software. A.V.L. Writing—original draft, Investigation. D.P.V.: Resources, Writing—review & editing, Methodology. S.T.: Supervision, Conceptualization, Writing—review & editing. All authors have read and agreed to the published version of the manuscript.

Data Availability Statement: The data presented in this study are available on request from the corresponding authors.

Conflicts of Interest: The authors declare no conflicts of interest.

References

1. Foppa, L.; Margossian, T.; Kim, S.M.; Müller, C.; Copéret, C.; Larmier, K.; Comas-Vives, A. Contrasting the Role of Ni/Al$_2$O$_3$ Interfaces in Water–Gas Shift and Dry Reforming of Methane. *J. Am. Chem. Soc.* **2017**, *139*, 17128–17139. [CrossRef] [PubMed]

2. Brandt, A.J.; Maddumapatabandi, T.D.; Shakya, D.M.; Xie, K.; Seuser, G.S.; Farzandh, S.; Chen, D.A. Water-gas shift activity on Pt-Re surfaces and the role of the support. *J. Chem. Phys.* **2019**, *151*, 234714. [CrossRef] [PubMed]

3. Kauppinen, M.M.; Korpelin, V.; Verma, A.M.; Melander, M.M.; Honkala, K. Escaping scaling relationships for water dissociation at interfacial sites of zirconia-supported Rh and Pt clusters. *J. Chem. Phys.* **2019**, *151*, 164302. [CrossRef] [PubMed]

4. Lozano-Reis, P.; Prats, H.; Sayós, R.; Rodriguez, J.A.; Illas, F. Assessing the Activity of Ni Clusters Supported on TiC(001) toward CO$_2$ and H$_2$ Dissociation. *J. Phys. Chem. C* **2021**, *125*, 12019–12027. [CrossRef]

5. Lozano-Reis, P.; Prats, H.; Sayós, R.; Illas, F. Limitations of free energy diagrams to predict the catalytic activity: The reverse water gas shift reaction catalyzed by Ni/TiC. *J. Catal.* **2023**, *425*, 203–211. [CrossRef]

6. Rodriguez, J.A.; Illas, F. Activation of noble metals on metal-carbide surfaces: Novel catalysts for CO oxidation, desulfurization and hydrogenation reactions. *Phys. Chem. Chem. Phys.* **2012**, *14*, 427–438. [CrossRef]

7. Lozano-Reis, P.; Sayós, R.; Rodriguez, J.A.; Illas, F. Structural, electronic, and magnetic properties of Ni nanoparticles supported on the TiC(001) surface. *Phys. Chem. Chem. Phys.* **2020**, *22*, 26145–26154. [CrossRef]

8. Vaarkamp, M.; Miller, J.T.; Modica, F.S.; Koningsberger, D.C. On the Relation between Particle Morphology, Structure of the Metal-Support Interface, and Catalytic Properties of Pt/γ-Al$_2$O$_3$. *J. Catal.* **1996**, *163*, 294–305. [CrossRef]

9. Yates, D.J.C.; Murell, L.L.; Prestridge, E.B. Ultradispersed rhodium rafts: Their existence and topology. *J. Catal.* **1979**, *57*, 41–63. [CrossRef]

10. PNellist, P.D.; Pennycook, S.J. Direct Imaging of the Atomic Configuration of Ultradispersed Catalysts. *Science* **1996**, *274*, 413–415. [CrossRef]

11. Kwak, J.H.; Hu, J.; Mei, D.; Yi, C.-W.; Kim, D.H.; Peden, C.H.F.; Allard, L.F.; Szanyi, J. Coordinatively Unsaturated Al^{3+} Centers as Binding Sites for Active Catalyst Phases of Platinum on γ-Al$_2$O$_3$. *Science* **2009**, *325*, 1670–1673. [CrossRef]

12. Van Zon, F.B.M.; Maloney, S.D.; Gates, B.C.; Koningsberger, D.C. Structure and nature of the metal-support interface: Characterization of iridium clusters on magnesium oxide by extended x-ray absorption fine structure spectroscopy. *J. Am. Chem. Soc.* **1993**, *115*, 10317–10326. [CrossRef]

13. Asakura, K.; Iwasawa, Y. Surface structure and catalysis for CO hydrogenation of the supported Ru species derived from the Ru$_3$(CO)$_{12}$ inorganic oxides. *J. Chem. Soc. Faraday Trans.* **1990**, *86*, 2657–2662. [CrossRef]

14. Fuentes, S.; Vázquez, A.; Pérez, J.; Yacamán, M. About the structure of small metal Rh particles on TiO$_2$: TEM study. *J. Catal.* **1986**, *99*, 492–497. [CrossRef]

15. Hansgen, D.A.; Vlachos, D.G.; Chen, J.G. Ammonia decomposition activity on monolayer Ni supported on Ru, Pt and WC substrates. *Surf. Sci.* **2011**, *605*, 2055–2060. [CrossRef]

16. Lai, X.; Clair, T.; Valden, M.; Goodman, D. Scanning tunneling microscopy studies of metal clusters supported on TiO2 (110): Morphology and electronic structure. *Prog. Surf. Sci.* **1998**, *59*, 25–52. [CrossRef]

17. Rybakov, A.A.; Larin, V.A.; Trubnikov, D.N.; Todorova, S.; Larin, A.V. Translational dependence of the geometry of metallic mono- and bilayers optimized on semi-ionic supports: The cases of Pd on γ-Al$_2$O$_3$(110), monoclinic ZrO$_2$(001), and rutile TiO$_2$(001). *CrystEngComm* **2021**, *24*, 143–155. [CrossRef]

18. Sanchez, J.; Koudelka, M.; Augustynski, J. Core-level chemical shift effect for platinum supported on TiO2film electrode. *J. Electroanal. Chem. Interfacial Electrochem.* **1982**, *140*, 161–166. [CrossRef]

19. Uribe, F.A.; Garzon, F.H.; Brosha, E.L.; Johnston, C.M.; Conradson, S.D.; Wilson, M.S. Spontaneous Deposition of Noble Metal Films onto Hexaboride Surfaces. *J. Electrochem. Soc.* **2007**, *154*, D623. [CrossRef]

20. Valden, M.; Lai, X.; Goodman, D.W. Onset of Catalytic Activity of Gold Clusters on Titania with the Appearance of Nonmetallic Properties. *Science* **1998**, *281*, 1647–1650. [CrossRef] [PubMed]

21. Chen, L.; Allec, S.I.; Nguyen, M.-T.; Kovarik, L.; Hoffman, A.S.; Hong, J.; Meira, D.; Shi, H.; Bare, S.R.; Glezakou, V.-A.; et al. Dynamic Evolution of Palladium Single Atoms on Anatase Titania Support Determines the Reverse Water–Gas Shift Activity. *J. Am. Chem. Soc.* **2023**, *145*, 10847–10860. [CrossRef]

22. Rybakov, A.A.; Bryukhanov, I.A.; Trubnikov, D.N.; Todorova, S.; Larin, A.V. Partial Palladium Oxidation over Various Oxide Supports for a Higher Reactivity of PdO with Respect to CH_4. *J. Phys. Chem. C* **2022**, *126*, 13132–13146. [CrossRef]

23. Wolniewicz, L. Vibrational—Rotational Study of the Electronic Ground State of the Hydrogen Molecule. *J. Chem. Phys.* **1966**, *45*, 515–523. [CrossRef]

24. Mao, J.; Li, S.; Zhang, Y.; Chu, X.; Yang, Z. Density functional study on the mechanism for the highly active palladium monolayer supported on titanium carbide for the oxygen reduction reaction. *J. Chem. Phys.* **2016**, *144*, 204703. [CrossRef] [PubMed]

25. Liu, N.; Mao, J.; Yang, Z. Mitigation of CO poisoning on functionalized palladium monolayer supported on titanium carbide. *Surf. Coat. Technol.* **2020**, *402*, 125925. [CrossRef]

26. Rybakov, A.A.; Todorova, S.; Trubnikov, D.N.; Larin, A.V. Reconstruction and catalytic activity of hybrid Pd(100)/(111) monolayer on γ-Al_2O_3(100) in CH_4, H_2O, and O_2 dissociation. *Dalton Trans.* **2021**, *50*, 8863–8876. [CrossRef]

27. Takahashi, K.; Hussain, T.; Takahashi, L.; Baran, J.D. Designing Square Two-Dimensional Gold and Platinum. *Cryst. Growth Des.* **2016**, *16*, 1746–1750. [CrossRef]

28. Czelej, K.; Cwieka, K.; Wejrzanowski, T.; Spiewak, P.; Kurzydlowski, K.J. Decomposition of activated CO_2 species on Ni(110): Role of surface diffusion in the reaction mechanism. *Catal. Commun.* **2016**, *74*, 65–70. [CrossRef]

29. Rodriguez, J.A.; Goodman, D.W. The Nature of the Metal-Metal Bond in Bimetallic Surfaces. *Science* **1992**, *257*, 897–903. [CrossRef] [PubMed]

30. Hammer, B.; Nørskov, J. Electronic factors determining the reactivity of metal surfaces. *Surf. Sci.* **1995**, *343*, 211–220. [CrossRef]

31. Hofmann, T.; Yu, T.H.; Folse, M.; Weinhardt, L.; Bär, M.; Zhang, Y.; Merinov, B.V.; Myers, D.J.; Goddard, W.A.; Heske, C. Using Photoelectron Spectroscopy and Quantum Mechanics to Determine d-Band Energies of Metals for Catalytic Applications. *J. Phys. Chem. C* **2012**, *116*, 24016–24026. [CrossRef]

32. Abild-Pedersen, F.; Nilsson, A.; Nørskov, J.K. Comment on "Using Photoelectron Spectroscopy and Quantum Mechanics to Determine d-Band Energies of Metals for Catalytic Applications". *J. Phys. Chem. C* **2013**, *117*, 6914–6915. [CrossRef]

33. Kresse, G.; Hafner, J. Ab initio molecular dynamics for liquid metals. *Phys. Rev. B* **1993**, *47*, 558–561. [CrossRef]

34. Kresse, G.; Furthmüller, J. Efficient iterative schemes for ab initio total-energy calculations using a plane-wave basis set. *Phys. Rev. B* **1996**, *54*, 11169–11186. [CrossRef]

35. Perdew, J.P.; Burke, K.; Ernzerhof, M. Generalized gradient approximation made simple. *Phys. Rev. Lett.* **1996**, *77*, 3865–3868. [CrossRef] [PubMed]

36. Kresse, G.; Joubert, D. From ultrasoft pseudopotentials to the projector augmented-wave method. *Phys. Rev. B* **1999**, *59*, 1758–1775. [CrossRef]

37. Grimme, S.; Antony, J.; Ehrlich, S.; Krieg, H. A consistent and accurate ab initio parametrization of density functional dispersion correction (DFT-D) for the 94 elements H-Pu. *J. Chem. Phys.* **2010**, *132*, 154104. [CrossRef]

38. Caldeweyher, E.; Mewes, J.-M.; Ehlert, S.; Grimme, S. Extension and evaluation of the D4 London-dispersion model for periodic systems. *Phys. Chem. Chem. Phys.* **2020**, *22*, 8499–8512. [CrossRef] [PubMed]

39. Henkelman, G.; Uberuaga, B.P.; Jónsson, H. A climbing image nudged elastic band method for finding saddle points and minimum energy paths. *J. Chem. Phys.* **2000**, *113*, 9901–9904. [CrossRef]

40. Voevodin, V.V.; Antonov, A.S.; Nikitenko, D.A.; Shvets, P.A.; Sobolev, S.I.; Sidorov, I.Y.; Stefanov, K.S.; Voevodin, V.V.; Zhumatiy, S.A. Supercomputer Lomonosov-2: Large Scale, Deep Monitoring and Fine Analytics for the User Community. *Supercomput. Front. Innov.* **2019**, *6*, 4–11. [CrossRef]